

Supplementary Materials

A Multifunctional Wearable Device with Graphene/Silver Nanowire Nanocomposite for Highly Sensitive Strain Sensing and Drug Delivery

Ge Shi¹, Tianqing Liu², Zlatko Kopecki³, Allison Cowin³, Ivan Lee⁴, Jing-Hong Pai⁵, Sean E. Lowe¹, Yu Lin Zhong^{1*}

¹ Centre for Clean Environment and Energy, School of Environment and Science, Gold Coast Campus, Griffith University, Gold Coast, Queensland 4222, Australia, ge.shi@griffith.edu.au, sean.lowe@griffithuni.edu.au

² QIMR Berghofer Medical Research Institute, Brisbane City QLD 4006, Australia, Michelle.Liu@qimrberghofer.edu.au

³ Future Industries Institute, University of South Australia, Mawson Lakes, SA 5095, Australia, Zlatko.Kopecki@unisa.edu.au, Allison.Cowin@unisa.edu.au

⁴ School of Information Technology and Mathematical Sciences University of South Australia, ivan.lee@unisa.edu.au

⁵ Australian National Fabrication Facility-South Australian Node, Future Industries Institute, University of South Australia, Mawson Lakes, SA 5095, Australia, Jing-Hong.Pai@unisa.edu.au

* Correspondence: Yulin Zhong. y.zhong@griffith.edu.au; Tel.: +61 7 555 28209

1. Schematic of the fabrication procedure of the PDMS micropillars

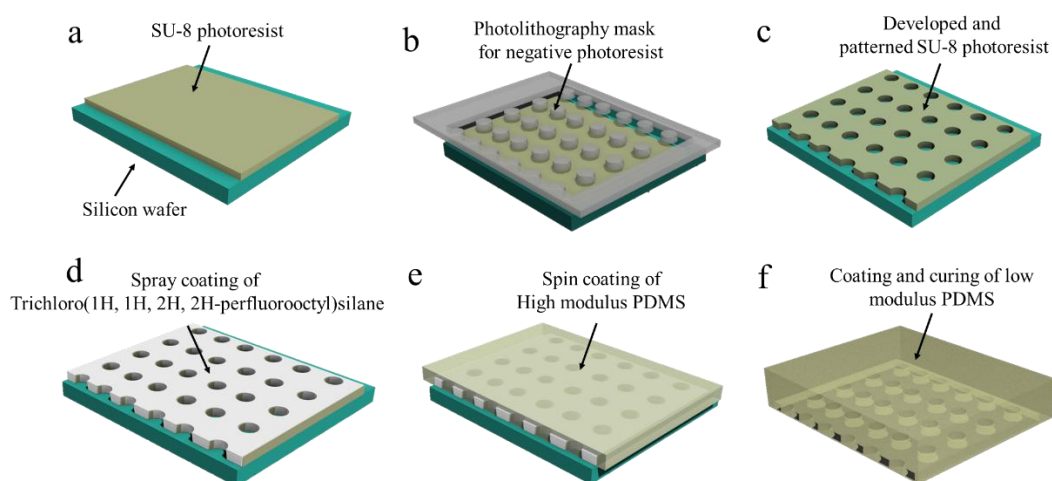


Figure S1. Schematic of the fabrication of micropillars through photolithography with an SU-8 film and a subsequent replica molding with PDMS.

The general fabrication process of PDMS micropillars is illustrated in Figure S1. It includes fabrication of an SU-8 template with microholes and coating of liquid PDMS precursor. Initially, SU-8 photoresist was spin coated on the silicon to produce a SU-8 film (Figure S1a). Then, the SU-8 film was exposed to UV light at passing a mask to form a microhole pattern (Figure S1b). After UV exposure, the SU-8 film was developed and baked again to produce a template with microholes (Figure S1c). Next, trichlorosilane solution was spray coated onto the SU-8 template (Figure S1d), onto which 400 mg high modulus PDMS (~2.81 MPa) was sequentially spin-coated, to form the micropillars (Figure S1e). The trichlorosilane grafted to hydroxyl moieties, rendering the surface hydrophobic[1]. With the spray coating of trichlorosilane, PDMS substrate can be easily peeled off. The high modulus micropillars can maintain their shape without leaning, bending or breaking with strain. After partial curing of the high modulus PDMS, 10 g low modulus PDMS (~2.58 MPa) was coated to form a soft substrate (Figure S1f). When the high modulus PDMS micropillars attach on skin, it would form a robust, adhesive interface with skin surface. At the same time, the low modulus PDMS film upon which the components are applied maintains flexibility.

2. Photograph and SEM micrographs of SU-8 template and PDMS substrate

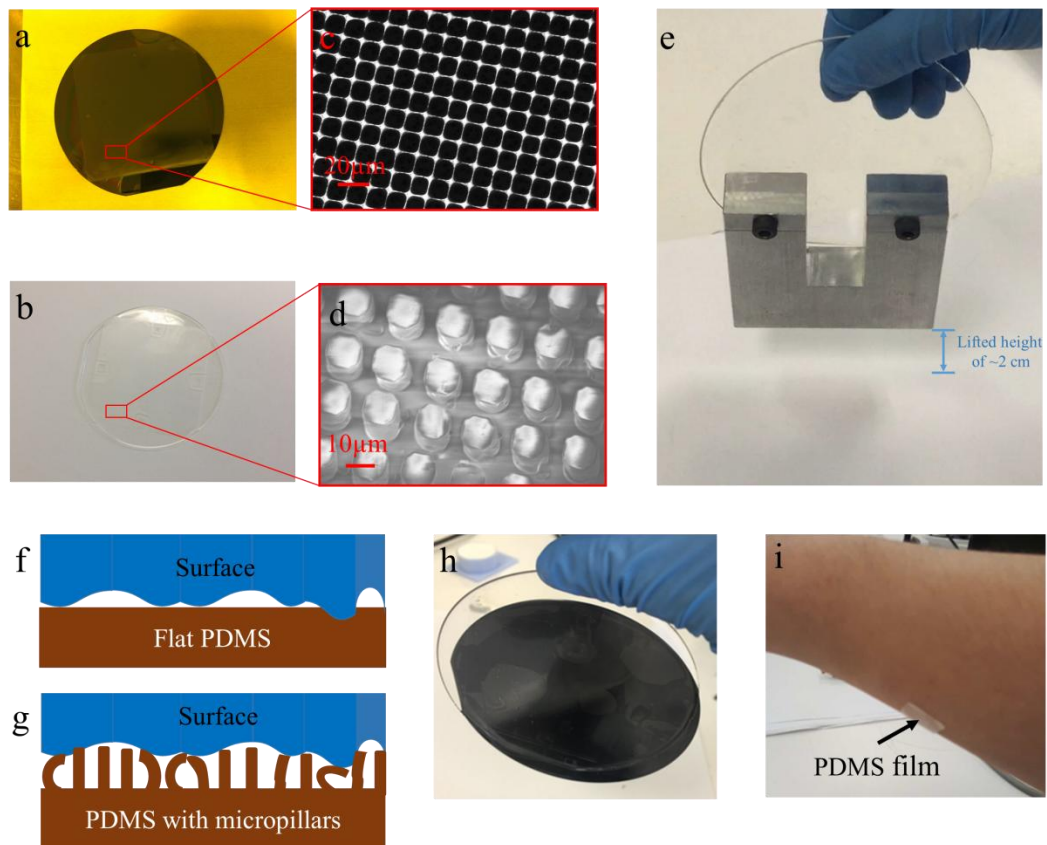


Figure S2. Digital photograph of (a) a silicon wafer with SU-8 template, b) PDMS substrate and e) a PDMS substrate that adhered and lifted an alloy block. SEM micrographs of c) the microholes in the SU-8 template and d) micropillars in the PDMS substrate. Schematic of the contact areas of f) flat substrate and of g) substrate with micropillars over rough surfaces. Digital photographs of h) PDMS film adhered onto silicon wafer and i) PDMS film (1 × 1 cm²) on human arm.

3. The cross-section of PDMS substrate

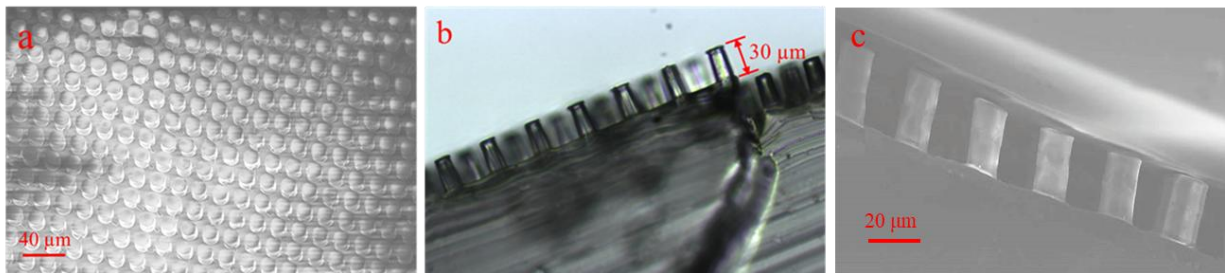


Figure S3. (a) SEM micrograph of PDMS substrate with the uniformly patterned array of micropillars, (b) optical image of the micropillar, (c) SEM micrograph of micropillars attached on a surface

Figure S3a shows an SEM micrograph of the PDMS substrate, which has a large number of uniformly arranged micropillars. Figure S3b shows a cross-sectional micrograph of the micropillars, which have an aspect ratio of $\sim 3:1$. Figure S3c shows the attachment of micropillars over a relatively rough surface.

4. Loading test of a small piece of PDMS substrate

1 cm² PDMS dry adhesive substrate

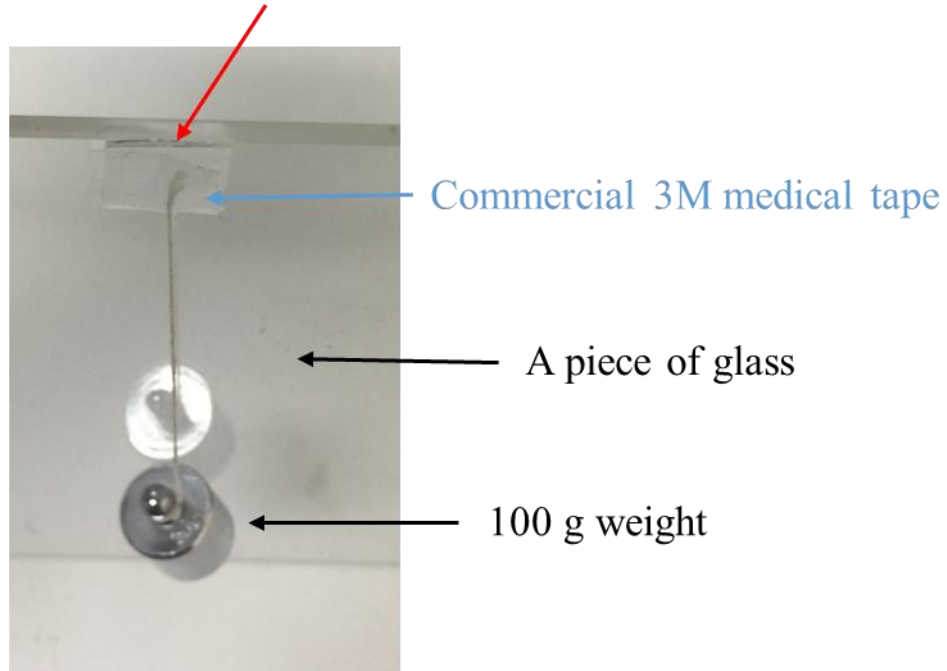


Figure S4. Digital photograph of a piece of PDMS dry adhesive sustaining loading from a poise weight. Figure S4 shows that 1 cm² PDMS dry adhesive substrate attached on a glass surface can easily sustain the load from a 100 g weight. The substrate is able to sustain the load for over two hours. Notably, if

the weight is greater than 100 g, the piece of commercial 3M medical tape peel off immediately. Thus, the adhesive force of the PDMS substrate exceeds that of the commercial 3M medical tape.

5. Characterization of graphene nanoplatelet

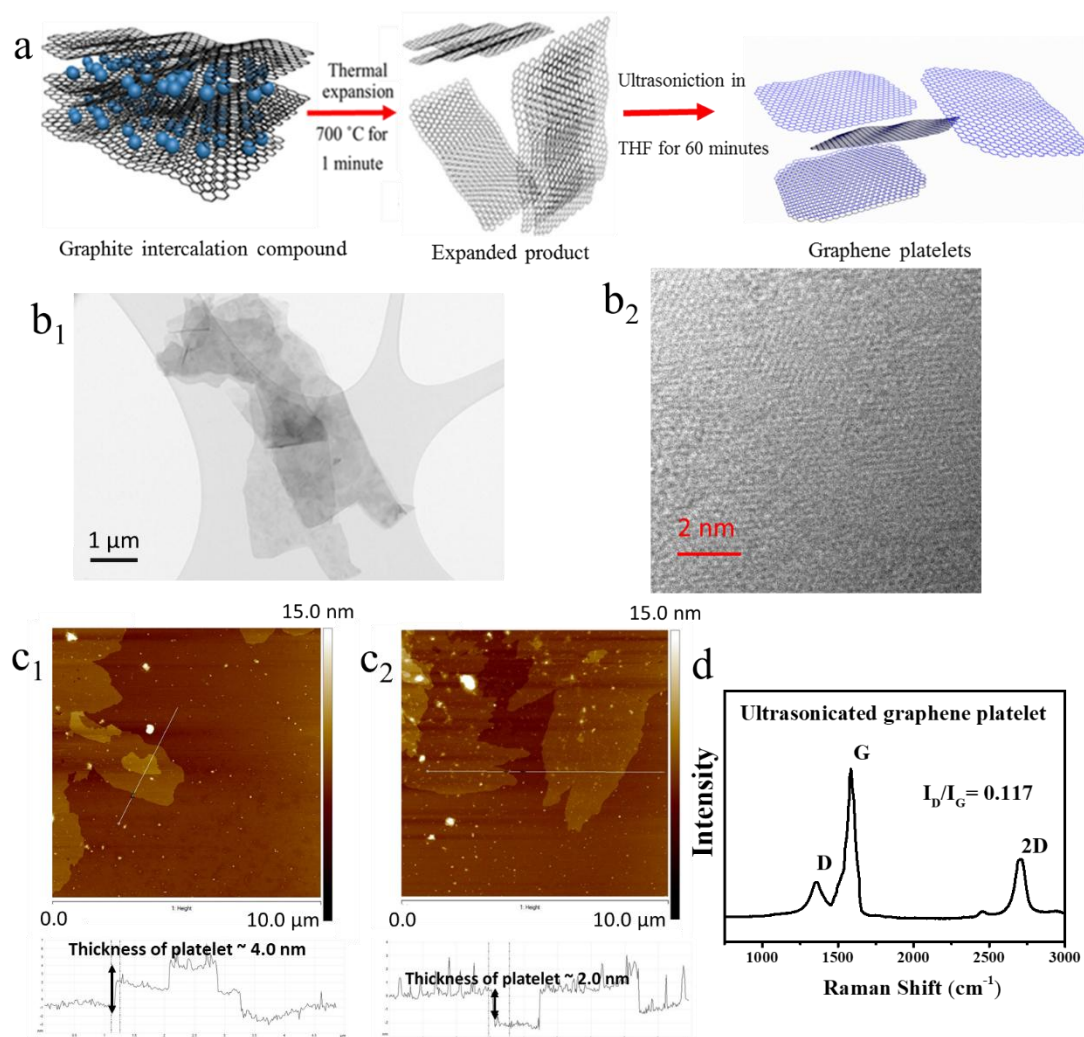


Figure S5. Characterization of graphene nanoplatelets. (a) Schematic showing the process of thermally expanding a graphite intercalation compound. b₁) TEM microscopy of a representative graphene nanoplatelet having lateral dimension $\sim 10 \mu\text{m}$ and b₂) high-magnification TEM image of a typical region from a randomly selected nanoplatelet. c) AFM micrographs of typical graphene nanoplatelets, and the related height profiles. d) Raman spectrum of GnPs.

Figure S5a schematically describes the fabrication of graphene nanoplatelets through thermal expansion of a commercial graphite intercalation compound (Asbury 1721) in a crucible at $700 \text{ }^\circ\text{C}$ for 1 min and following ultrasonication. The thermally expanded product then underwent ultrasonication in tetrahydrofuran (THF) for 60 minutes to produce thinner graphene nanoplatelets (GnPs). The TEM micrograph in Figure S5 b₁ show the few layer structure of a graphene nanoplatelet. The high

magnification TEM micrograph in Figure S5 b₂ indicates the highly crystalline structure of the graphene nanoplatelet. Atomic force microscopy (AFM) measurements (Figure S5 c₁ and c₂) indicated a thickness of 2.0 – 5.0 nm. In Figure S5d, a Raman spectrum shows three prominent peaks at 1350, 1579 and 2700 cm⁻¹, corresponding to D, G and 2D bands, respectively. The low I_D/I_G ratio of 0.117 implies the high structural integrity of GnPs.

6. Silver nanowire

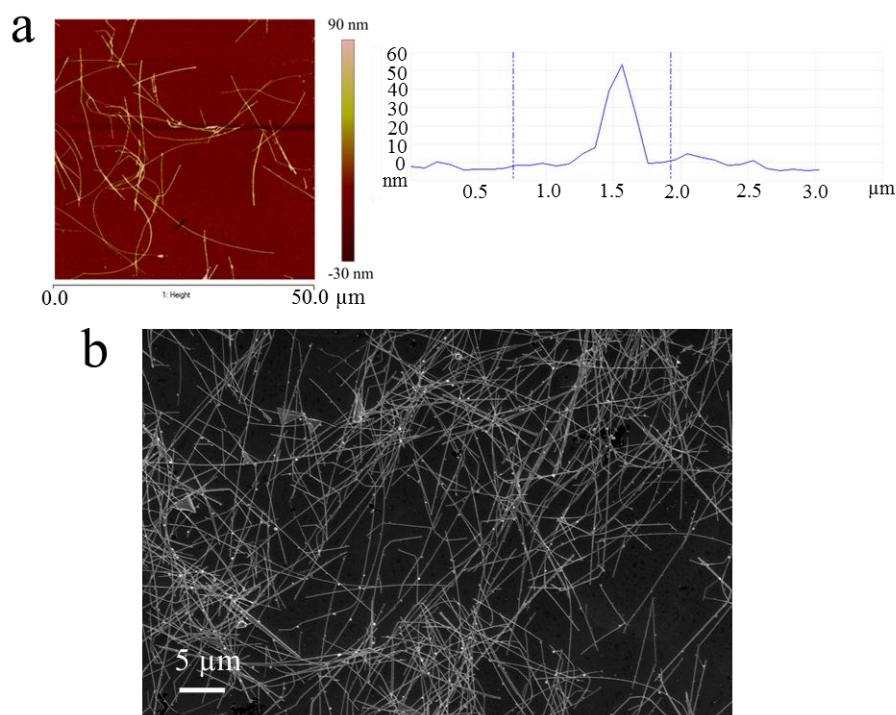


Figure S6. Characterization of silver nanowires. (a) AFM micrography and b) SEM micrograph of silver nanowires.

Silver nanowires (AgNW-40) were purchased from ACS material. As shown in Figure S6a, AgNWs have diameter of 40 nm. The SEM micrograph in Figure S6b indicates the AgNWs have lengths of 20–60 μm .

7. Schematic of a “filtration-patterning” method

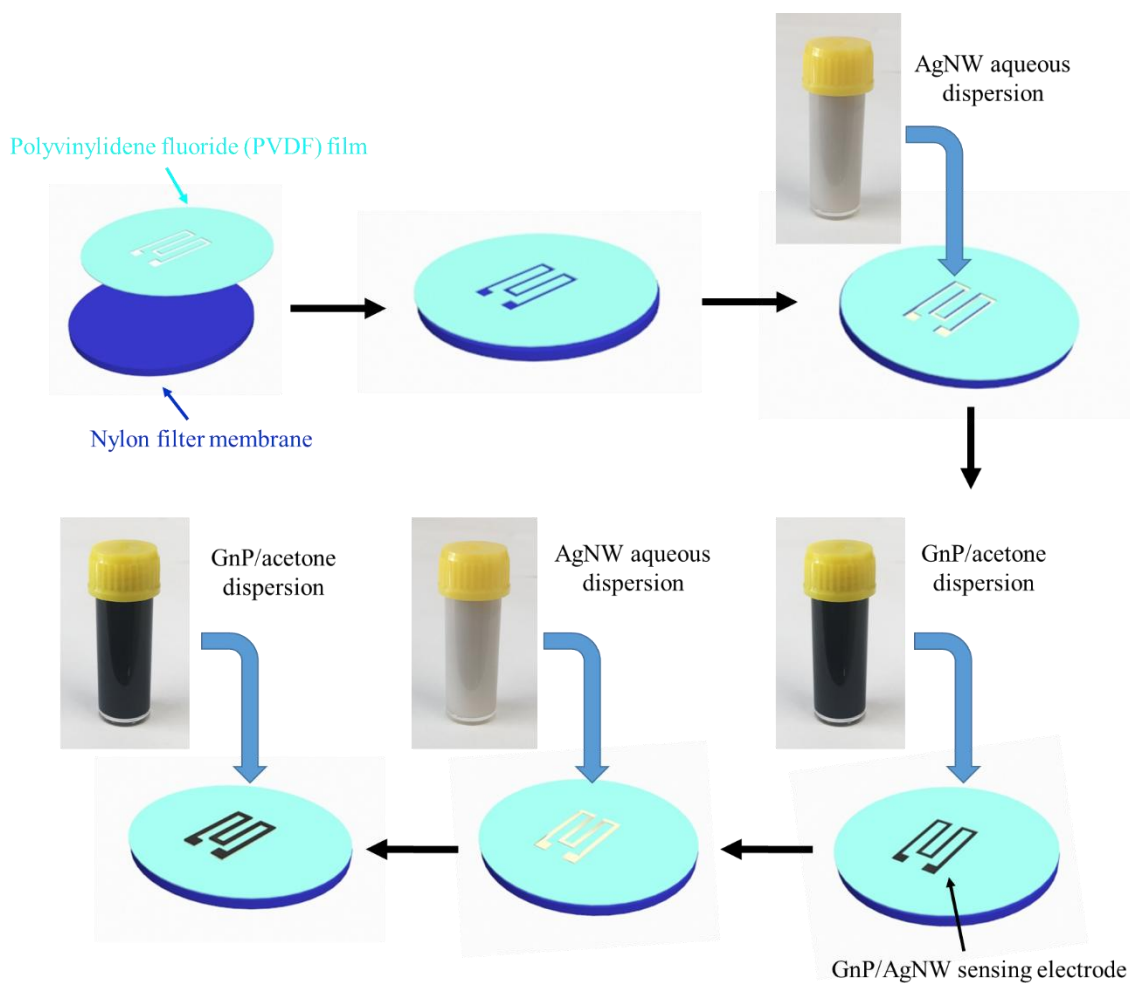


Figure S7 Schematic of a “filtration-patterning” method.

Figure S7 shows the schematic of a “filtration-patterning” method. Using vacuum filtration, GnP and AgNWs dispersion were alternately deposited on filter paper, creating a sandwich-structured GnP/Ag film whose geometry is similar to the pattern on the PVDF film.

8. Fabricate process of the sensor composite

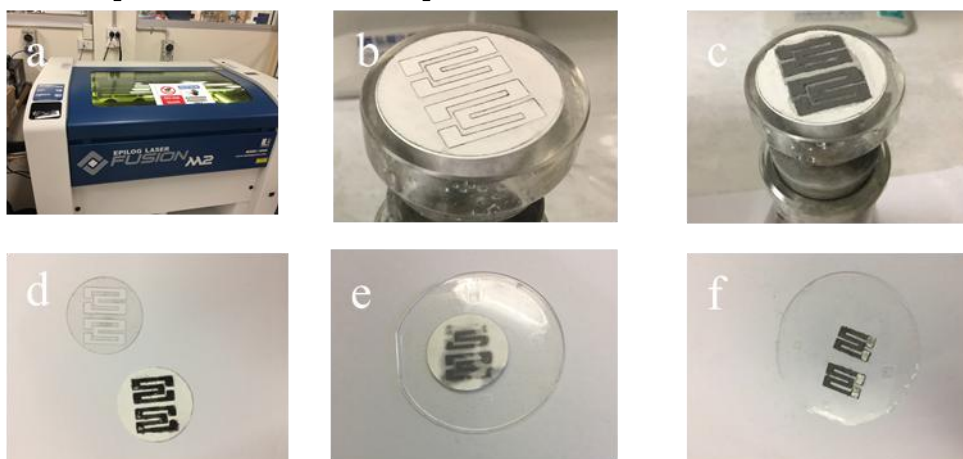


Figure S8. Fabrication of strain sensors using GnP/AgNW composite and PDMS substrate. Digital photographs of a) a laser cutter to create a pattern on PET film, b) placing the film on filtration paper, c) forming a pattern of GnP/AgNW composite on the paper, d) adding PDMS onto the pattern and peeling off PET film, e) moving filtration paper onto micropillar substrate and f) peeling off filtration paper.

Firstly, a pattern was made in a polyethylene terephthalate (PET) film through laser cutting (Figure S8a), and the film was placed on a piece of filtration paper (Figure S8b). Under vacuum condition, ~10 g of GnP/acetone solution at 0.5 mg/ml and ~10 g Ag nanowire aqueous solution at 0.1 mg/ml were alternately filtrated through the film and filtration paper, creating a sandwich-structured GnP/Ag film whose geometry is similar to the pattern on the PET film (Figure S8c). PDMS oligomer was poured onto and permeated into the GnP/Ag film (Figure S8d). Prior to the curing of PDMS, the PET film was peeled off, leaving the GnP/Ag pattern on the filtration paper. The paper was turn over and attached onto the micropillar substrate (Figure S8e). After curing and removal of the filtration paper, the GnP/Ag pattern was bonded with Ag paste and Ag wires as a sensor (Figure S8f).

9. SEM micrograph of a PDMS encapsulated GnP/AgNW sandwich composite

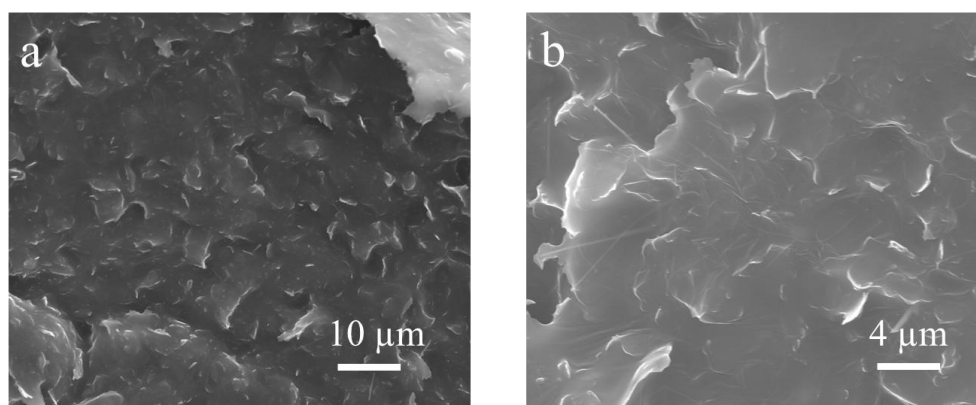


Figure S9. SEM micrographs of cross-section region of a PDMS encapsulated GnP/AgNW sandwich composite.

Figure S9a shows that the SEM micrographs of the cross-section region of a GnP/AgNW sandwich composite which is encapsulated by PDMS. As shown in Figure S9b, the dispersion of AgNW and GnPs in PDMS matrix can be clearly observed in Figure S9b.

10. Resistance change of AgNW and Graphene nanoplatelet as a function of tensile strain

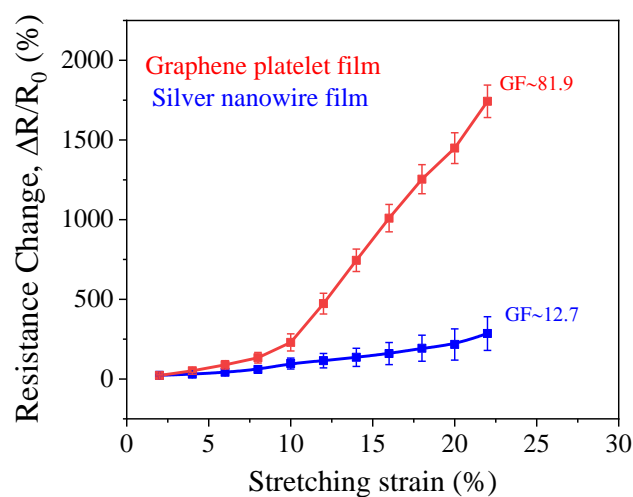


Figure S10. Resistance change ($\Delta R/R_0$) as a function of tensile strain with graphene nanoplatelet/silver nanowire film sensor with thickness of $\sim 30 \mu\text{m}$.

Figure S10 shows the resistance changes and gauge factors of the graphene nanoplatelet and silver nanowire sensors as a function of tensile strain. The sensitive films were prepared by similar “filtration-patterning” method and have thickness of $\sim 40 \mu\text{m}$. After filtration, the AgNWs were tightly stacked and tangled together. Thus the film exhibited a low gauge factor and linear response to strain. The GnP

film still consists of microcracks and micropores, so after 10% tensile strain, the film exhibited a high gauge factor of 81.9, and the resistance increased rapidly. This is because at such strain, most of GnP's should stretch and slide past each other, which leads to more numerous and larger microcracks.

11. Response time of sensors

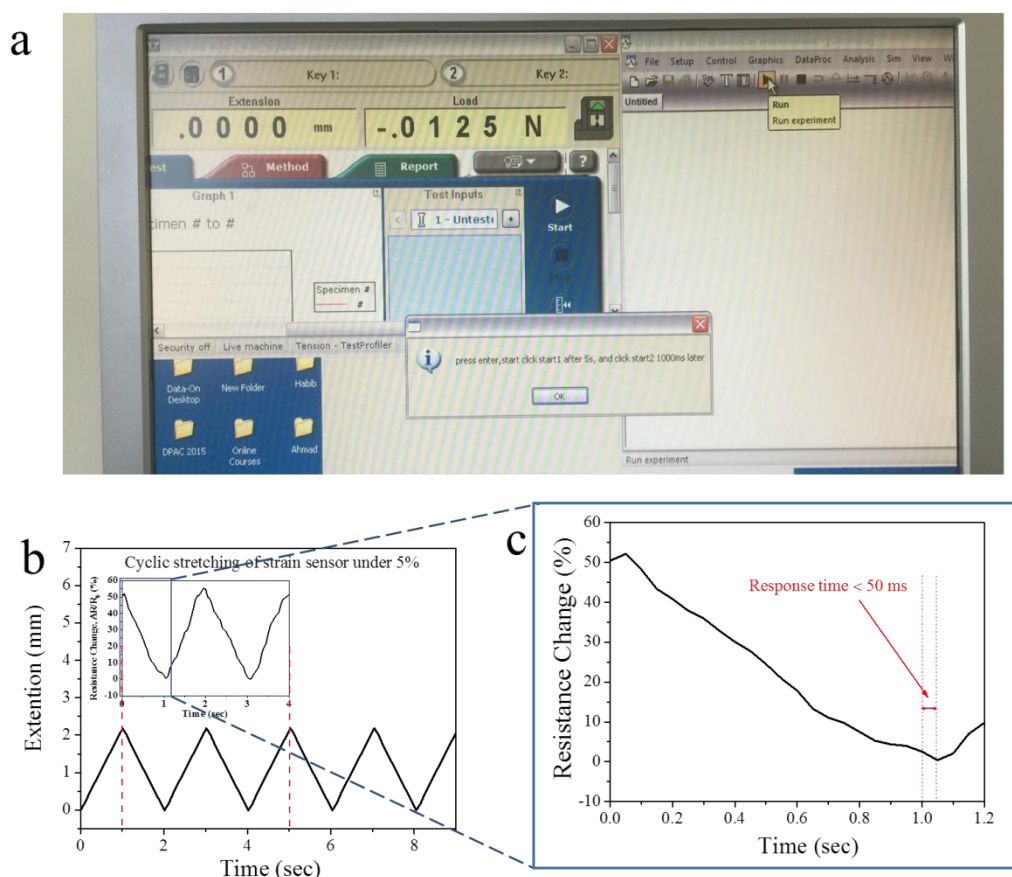


Figure S11. (a) Photograph of the suite of three programs used to obtain response time, b) resistance change ($\Delta R/R_0$) and tensile extension over time at a frequency of two second per cycle and c) the response time of the sensor.

The response time was tested by using three different programs simultaneously: a custom-made program (middle window in Figure S11a) for controlling mouse clicks, Blue hills 2 (left window in Figure S11a) for Instron and the CHI potentiostat software (right window in Figure S11a) for recording resistance change. As shown in the pop-up window in the middle of Figure S11a, the tensile testing first activates and after 1000 milliseconds, the resistance change starts to be recorded. By comparing the tensile and electrical performance in Figure S11b, we found that the response time was less than 50 milliseconds, as indicated in Figure S11c.

12. Comparison of GnP/AgNW strain sensor with other piezoresistive strains sensor

Table S1. Comparison of the performances of piezoresistance type strain sensors and GnP/AgNW sensor.

Materials	Durability of sensors	Fabrication method	Gauge factor	Reported Minimum strain	Reference and publishing year
GnP/AgNW-PDMS	1000 cycles	Patterning filtration	12.6 –65.1	Wrist pulse	This work
Carbon nanotube-Ecoflex	3 cycles	Mixing	0.54–64	Finger bending	[3] 2015
Graphite slice-paper	12 cycles	Pencil drawing	60–150	Finger bending	[4] 2015
Electrochemical exfoliated graphene- PDMS	5 cycles	Coating on PDMS	228–1037	Wrist pulse	[5] 2016
Graphene nanoplatelets-medical tape	1000 cycles	Pressing on medical tape	27.7–164.5	Wrist pulse	[6] 2016
Electrochemical exfoliated graphene -PDMS	100,000 cycles	Self-aligned onto PDMS	115	Wrist pulse	[7] 2017
Silver nanowire/Gold nanowire-PDMS	1000 cycles	Embedding inside PDMS	5–236.6	Eyebrows motion	[8] 2017
Graphene textile-	500 cycles	Dipping polyester fabric into graphene oxide dispersion	1.7–26	Wrist pulse	[9] 2018
Cellulose fibers-paper	10,000 cycles	Coating cellulose fiber on paper	0.14–3.69	Wrist bending	[10] 2018

13. Human hand artery system

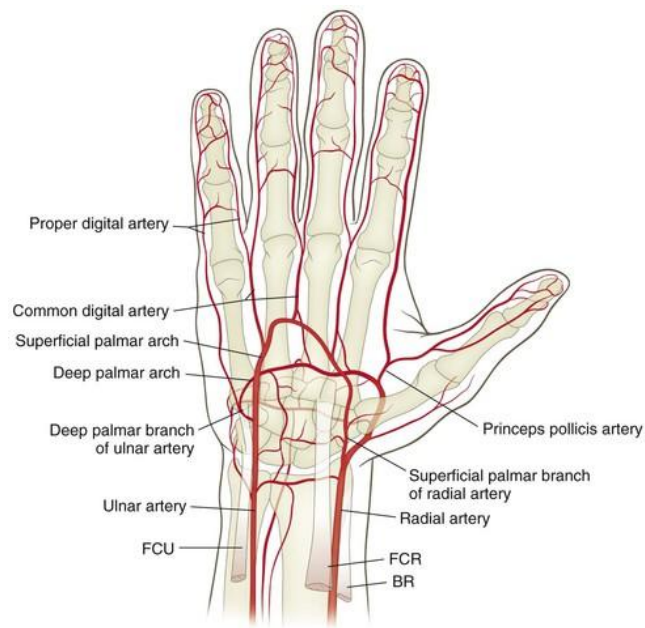


Figure S12. Schematic image of the system of arteries in the human hand

Figure S12 shows the arteries of the human hand, including the location of the ulnar artery and radial artery in the wrist.

14. Evaluation of cardiovascular condition

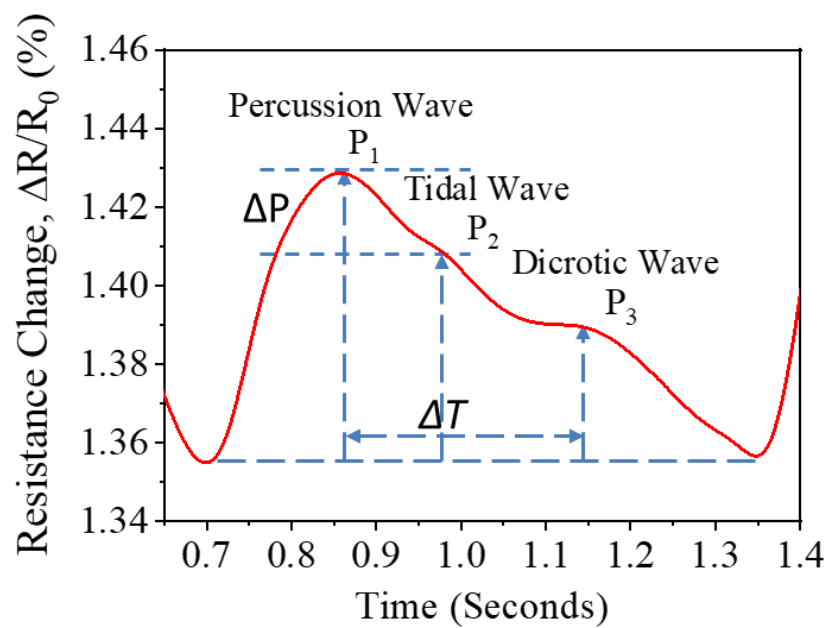


Figure S13 Waveform of a radial artery pulse

As shown in Figure S10, an enlarged pulse signal exhibits the characteristic peaks of radial waveforms, which contain important physiological information, including arterial stiffness, markers of coronary artery disease and myocardial infraction. Under normal condition, peak P_1 , P_2 , and P_3 indicate the percussion wave, tidal wave and dicrotic wave, respectively. Generally, there are two parameters are used to evaluate the physiological conditions of the cardiovascular system[2]: the augmentation index AI ($AI = \Delta P / P_1$, where $\Delta P = (P_1 - P_2)$, P_1 is the absolute pulse wave magnitude, equal to the height of the percussion wave peak, P_2 is the height of tidal wave peak) and the reflection index RI ($RI = h / \Delta T$, where h is the body height of the subject and ΔT is the time interval between P_1 and P_3). According to the data in Figure S10, the AI and RI were calculated to be $\sim 25.4\%$ and $\sim 5.5 \text{ ms}^{-1}$. This result demonstrates that the strain sensor has potential to be utilized in diagnostic applications.

15. Strain sensors used as E-skin to monitor movement of a field cricket and a wild snail.

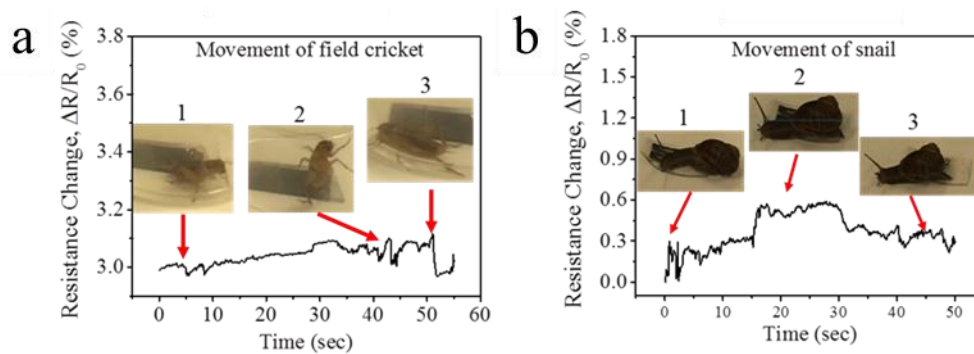


Figure S14. Application of strain sensor as an electronic skin to monitor movement of (a) a field cricket and (b) a wild snail.

Figure S14a demonstrates that a small cricket of $\sim 300 \text{ mg}$ in mass was walking on the skin, which may create a minor pressure below 10 Pa . The resistance decreases immediately when the whole body moved away from the skin (inset image 1); resistance increases promptly and sharply as long as one leg stamps on the skin (inset image 2). When the cricket fell from the container wall down to the skin, it created a large resistance change of $\sim 3.1\%$. The many minor resistance peaks relating to the cricket's slight, tiny motions. Slight strain caused by a wild snail was monitored. As shown in Figure S14b, the resistance changes immediately when the snail's head reaches the sensor (inset image 1). When it was creeping over the sensor, its foot leads to many minor peaks (inset image 2). As it was moving away, the resistance was gradually reduced (inset image 3).

16. The advantages and fabrication procedures of PLGA nanoparticles based drug delivery system

Chitosan hydrogels have been widely used as wound healing agent and have great potential for transdermal drug delivery [11-13]. Chitosan possesses the advantage of being biodegradable, biocompatible, good adhesion to a range of substrates and water permeable properties[14]. The chitosan encapsulates the PLGA nanoparticle vessels. PLGA consists of hydrophilic glycolic acid chains and less hydrophilic lactic acid blocks on the chain which can load either hydrophilic or hydrophobic drugs. Thus it can be used as a versatile drug carrier. Polymeric nanoparticle-encapsulated drugs are usually more effective than their freely delivered counterparts, as the protection from polymer encapsulation can enable slow release of the drug, longer biological half-life and the potential for reduced side effects [15-17]. DFO is an iron chelator used to reduce iron-induced oxidative damage in diseases which abnormally increase iron levels, such as β -thalassemia. It has also been demonstrated to have skin localized therapeutic benefits[18,19]. Therefore, we selected DFO as a model drug for this study. The preparation procedure of the transdermal drug delivery system include a double emulsion method to synthesis PLGA nanoparticles and to fabricate chitosan hydrogels as shown in Figure S15.

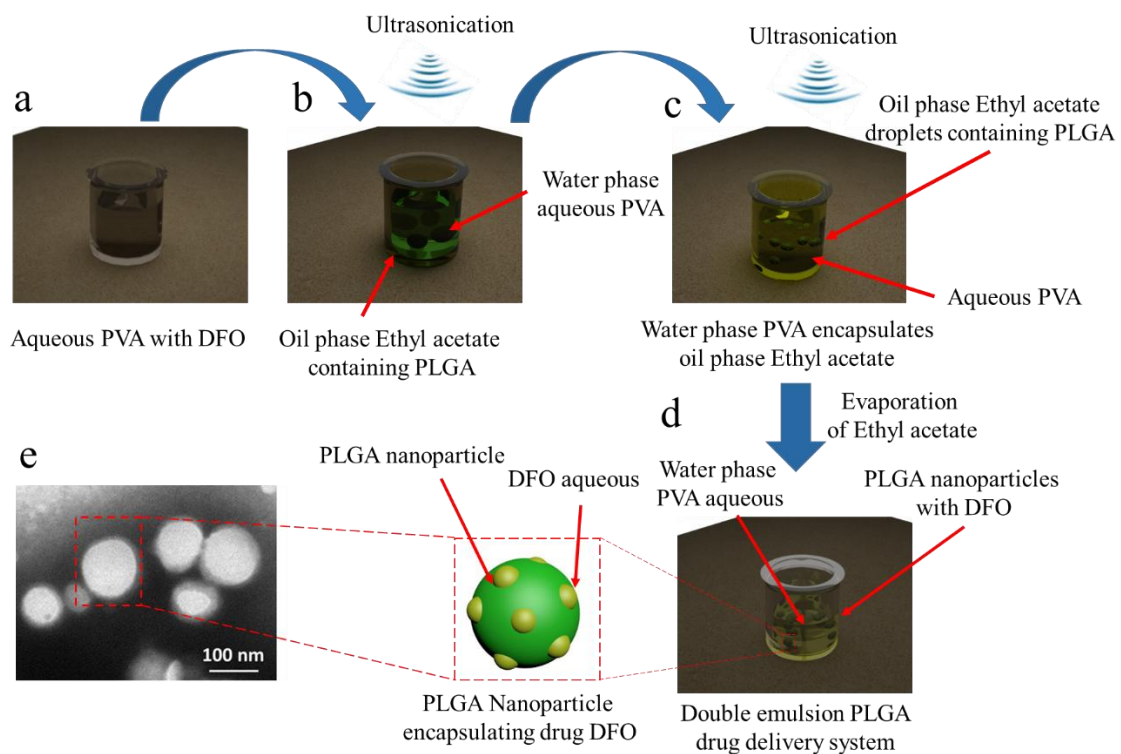


Figure S15. Schematic of fabrication process of chitosan-PLGA drug delivery system. a-d) Water-oil-water double emulsion fabrication process of PLGA nanoparticles inside aqueous PVA and e) TEM micrograph of PLGA nanoparticles.

Firstly, hydrophilic DFO is dissolved in PVA aqueous solution to form a water phase solution (Figure S12a). Secondly, the PVA solution with DFO was emulsified within ethyl acetate containing PLGA through ultrasonication, resulting in an oil/water emulsion (Figure S12b). In this emulsion, the DFO was encapsulated within the oil phase PLGA polymeric chains. Thirdly, the oil/water emulsion was added into PVA aqueous solution, resulting in a water/oil/water phase double emulsion (Figure S12c). Through ultrasonication in this emulsion, the oil phase ethyl acetate were separated as droplets and entrapped within the outside aqueous phase and form (Figure S12c). After evaporation of the volatile ethyl acetate, the PLGA chains are highly cross-linked with PVA acting as stabilizer. The aqueous solvent diffuses out, resulting in the PLGA nanoparticles encapsulated DFO (Figure S12d). TEM micrograph indicates that most PLGA nanoparticles have a diameter of ~80 nm (Figure S12e).

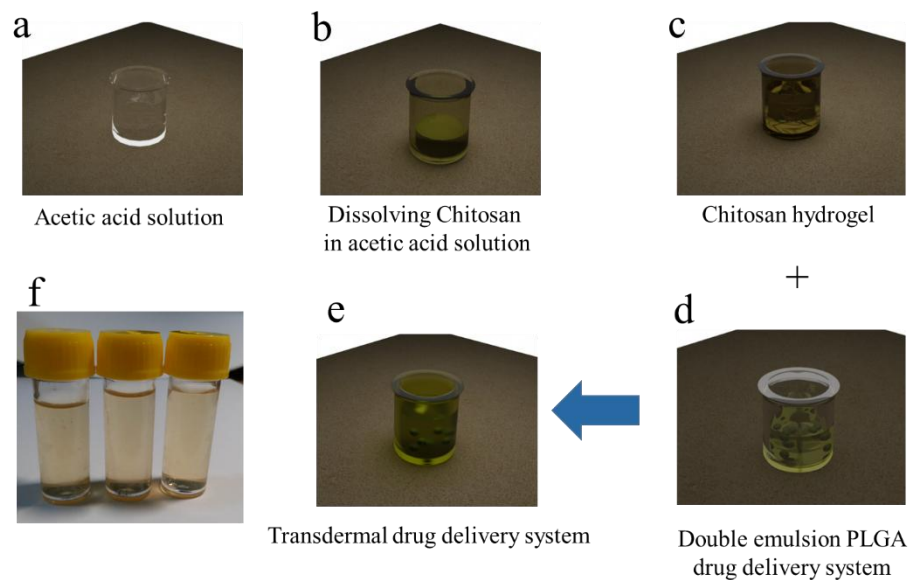


Figure S16. a–c) fabrication process of the chitosan hydrogel, d and e) of the final transdermal drug delivery system and f) digital photo of the hydrogel used for transdermal drug delivery.

Then, a chitosan hydrogel was prepared dissolve chitosan powder in acetic acid solution (Figure S13a) with concentrations of 1% v/v (Figure S13b) and incubated in a water bath for 3 hours at 55°C to synthesis chitosan hydrogel (Figure S13c). Lastly, the previous double emulsion solution (Figure S13d) was added and mixed within the chitosan hydrogel solution to produce the DFO-PLGA nanoparticles-chitosan system (Figure S13e). The digital photo of the system is shown in Figure S13f.

17. Digital photograph of a sensor with hydrogel drug delivery system

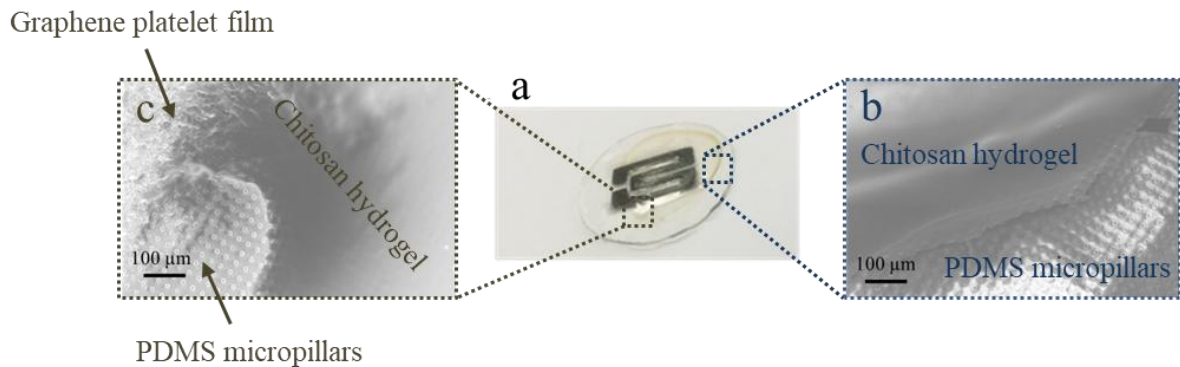


Figure S17. (a) Digital photograph of a multifunctional strain sensor loaded with the deferoxamine-PLGA-chitosan hydrogel transdermal drug delivery system. SEM micrographs of the sensor surfaces with b) chitosan hydrogel and PDMS micropillar substrate, and c) chitosan hydrogel, sensor component and PDMS micropillar array.

A droplet of chitosan hydrogel was deposited on the sensor. After water evaporation, a sticky film of the chitosan hydrogel was left on the sensor (Figure S17a). SEM micrographs in Figure S17 b and c show the surface morphology of the sensor.

18. Skin-on-a-chip model for DFO delivery

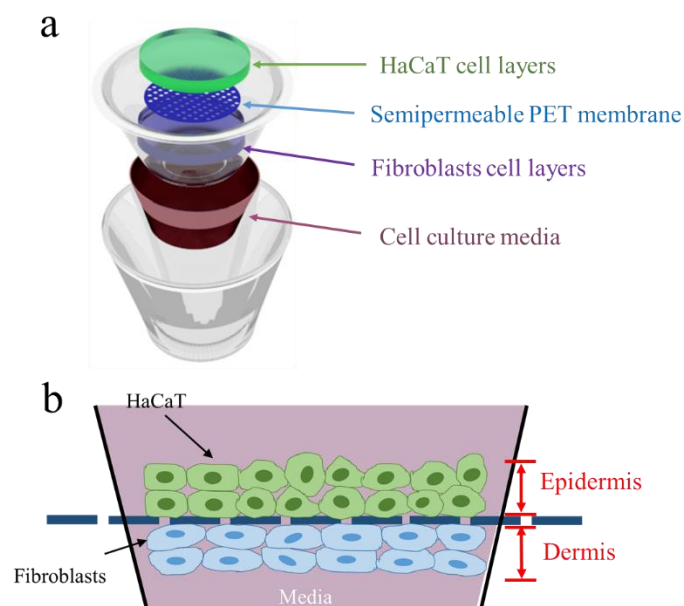


Figure S18. (a) Schematic of the skin-on-a-chip model based on a transwell chamber for DFO delivery assessment. (b) Schematic of the cross section of the cell layers on the transwell membrane.

As shown in Figure S18a, the model was developed based on cell transwell chambers, which consist of two cell layers of keratinocytes and skin fibroblasts and a transparent semipermeable polycarbonate

membrane which separates the apical and basolateral compartments. Firstly, media was added to the chamber as shown in Figure S18a. Secondly, keratinocytes and fibroblast cells were respectively seeded onto the upper and bottom surface of the PET membrane, and the cells were incubated overnight to encourage the cells to adhere to the membrane (Figure S18b). Lastly, the system was put into oven where the cells were cultured until reaching confluence, after which they can mimic the epithelial and endothelial barriers of skin. Specifically, keratinocytes and skin fibroblasts mimic the epidermis and dermis of physiological adult skin, respectively. Each cell layer was separated by transparent porous PET membranes to allow interlayer communication. Following the formation of an intact cellular membrane, the sensor was applied on the top surface of a HaCaT cellular layer.

19. Digital photograph of the skin penetration testing of cut sensor pieces

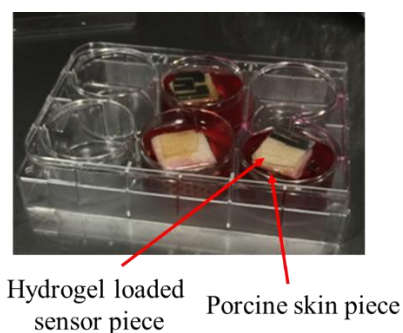


Figure S19. Photograph of the skin penetration testing used with the transdermal drug delivery system.

A photograph of the skin penetration testing apparatus is shown in Figure S19. A number of sensors, each $1 \times 1 \text{ cm}^2$, are placed onto the porcine skin piece to mimic the transdermal drug delivery process.

Reference

1. Bubendorfer, A.; Liu, X.; Ellis, A.V. Microfabrication of PDMS microchannels using SU-8/PMMA moldings and their sealing to polystyrene substrates. *Smart Materials and Structures* **2007**, *16*, 367.
2. Wilkinson, I.B.; Fuchs, S.A.; Jansen, I.M.; Spratt, J.C.; Murray, G.D.; Cockcroft, J.R.; Webb, D.J. Reproducibility of pulse wave velocity and augmentation index measured by pulse wave analysis. *Journal of hypertension* **1998**, *16*, 2079-2084.
3. Ryu, S.; Lee, P.; Chou, J.B.; Xu, R.; Zhao, R.; Hart, A.J.; Kim, S.-G. Extremely elastic wearable carbon nanotube fiber strain sensor for monitoring of human motion. *ACS nano* **2015**, *9*, 5929-5936.
4. Liao, X.; Liao, Q.; Yan, X.; Liang, Q.; Si, H.; Li, M.; Wu, H.; Cao, S.; Zhang, Y. Flexible and highly sensitive strain sensors fabricated by pencil drawn for wearable monitor. *Advanced Functional Materials* **2015**, *25*, 2395-2401.
5. Li, X.; Yang, T.; Yang, Y.; Zhu, J.; Li, L.; Alam, F.E.; Li, X.; Wang, K.; Cheng, H.; Lin, C.T. Large-Area Ultrathin Graphene Films by Single-Step Marangoni Self-Assembly for Highly Sensitive Strain Sensing Application. *Advanced Functional Materials* **2016**, *26*, 1322-1329.

6. Shi, G.; Zhao, Z.; Pai, J.H.; Lee, I.; Zhang, L.; Stevenson, C.; Ishara, K.; Zhang, R.; Zhu, H.; Ma, J. Highly Sensitive, Wearable, Durable Strain Sensors and Stretchable Conductors Using Graphene/Silicon Rubber Composites. *Advanced Functional Materials* **2016**.
7. Park, Y.; Shim, J.; Jeong, S.; Yi, G.R.; Chae, H.; Bae, J.W.; Kim, S.O.; Pang, C. Microtopography-guided conductive patterns of liquid-driven graphene nanoplatelet networks for stretchable and skin-conformal sensor array. *Advanced Materials* **2017**, *29*, 1606453.
8. Ho, M.D.; Ling, Y.; Yap, L.W.; Wang, Y.; Dong, D.; Zhao, Y.; Cheng, W. Percolating network of ultrathin gold nanowires and silver nanowires toward “invisible” wearable sensors for detecting emotional expression and apexcardiogram. *Advanced Functional Materials* **2017**, *27*, 1700845.
9. Yang, Z.; Pang, Y.; Han, X.-l.; Yang, Y.; Ling, J.; Jian, M.; Zhang, Y.; Yang, Y.; Ren, T.-L. Graphene Textile Strain Sensor with Negative Resistance Variation for Human Motion Detection. *ACS nano* **2018**, *12*, 9134-9141.
10. Chen, S.; Song, Y.; Ding, D.; Ling, Z.; Xu, F. Flexible and Anisotropic Strain Sensor Based on Carbonized Crepe Paper with Aligned Cellulose Fibers. *Advanced Functional Materials* **2018**, *28*, 1802547.
11. Boateng, J.S.; Matthews, K.H.; Stevens, H.N.; Eccleston, G.M. Wound healing dressings and drug delivery systems: a review. *Journal of pharmaceutical sciences* **2008**, *97*, 2892-2923.
12. Murakami, K.; Aoki, H.; Nakamura, S.; Nakamura, S.-i.; Takikawa, M.; Hanzawa, M.; Kishimoto, S.; Hattori, H.; Tanaka, Y.; Kiyosawa, T. Hydrogel blends of chitin/chitosan, fucoidan and alginate as healing-impaired wound dressings. *Biomaterials* **2010**, *31*, 83-90.
13. Ribeiro, M.P.; Espiga, A.; Silva, D.; Baptista, P.; Henriques, J.; Ferreira, C.; Silva, J.C.; Borges, J.P.; Pires, E.; Chaves, P. Development of a new chitosan hydrogel for wound dressing. *Wound repair and regeneration* **2009**, *17*, 817-824.
14. Vignesh, S.; Sivashanmugam, A.; Annapoorna, M.; Janarthanan, R.; Subramania, I.; Jayakumar, R. Injectable deferoxamine nanoparticles loaded chitosan-hyaluronic acid coacervate hydrogel for therapeutic angiogenesis. *Colloids and Surfaces B: Biointerfaces* **2018**, *161*, 129-138.
15. Wei, H.; Zhuo, R.-X.; Zhang, X.-Z. Design and development of polymeric micelles with cleavable links for intracellular drug delivery. *Progress in polymer Science* **2013**, *38*, 503-535.
16. Ulbrich, K.; Hola, K.; Subr, V.; Bakandritsos, A.; Tucek, J.; Zboril, R. Targeted drug delivery with polymers and magnetic nanoparticles: covalent and noncovalent approaches, release control, and clinical studies. *Chemical reviews* **2016**, *116*, 5338-5431.
17. Lowe, S.; O'Brien-Simpson, N.M.; Connal, L.A. Antibiofouling polymer interfaces: poly (ethylene glycol) and other promising candidates. *Polymer Chemistry* **2015**, *6*, 198-212.
18. Duscher, D.; Neofytou, E.; Wong, V.W.; Maan, Z.N.; Rennert, R.C.; Inayathullah, M.; Januszyk, M.; Rodrigues, M.; Malkovskiy, A.V.; Whitmore, A.J. Transdermal deferoxamine prevents pressure-induced diabetic ulcers. *Proceedings of the National Academy of Sciences* **2015**, *112*, 94-99.
19. Rasso, G.; Salis, A.; Porcu, E.P.; Giunchedi, P.; Roldo, M.; Gavini, E. Composite chitosan/alginate hydrogel for controlled release of deferoxamine: a system to potentially treat iron dysregulation diseases. *Carbohydrate polymers* **2016**, *136*, 1338-1347.